Validation of and Simulations using a High-Temperature Electrolysis Model

M. Nohl[a], I. C. Vinke[a], R.-A. Eichel[a,b], and L. G. J. de Haart[a]

[a] Institute of Energy and Climate Research, Fundamental Electrochemistry (IEK-9), Forschungszentrum Jülich GmbH, 52425 Jülich, Germany
[b] Department of Physical Chemistry IESW, RWTH Aachen University, 52074 Aachen, Germany

A continuum mechanistic, real-scale model with the most important reactions of high-temperature electrolysis is proposed. IV-characteristics and impedance spectra serve as comparison to experimental data for steam, CO_2 and co-electrolysis. The exchange current-density i_0 can be determined to the same order of magnitude as observed in experiments for steam electrolysis. The IV-characteristics for CO_2 electrolysis are well described by an i_0 one order of magnitude lower as compared to steam electrolysis. Parameter variations identify contributing variables determining the shapes of characteristics. Limitations in prediction are revealed for low current densities up to 0.5 $A \cdot cm^{-2}$. EIS calculations demonstrate the dominant behavior of charge transfer or oxygen ion incorporation into the lattice as function of i_0 or temperature. The model forms a solid basis for various future investigations like a more detailed reaction system with possible intermediates or degradation and poisoning effects.

Introduction

Efforts for increasing the share of renewable power generation are dramatically boosted since the start of the energy transition (1). Therefore, efficient conversion systems are of great importance to conserve most of the delivered power by nature. High-temperature electrolysis is such an efficient type of energy conversion system compared to similar technologies (2-4). To bridge the gap to an industrial scale application, the electrochemical and chemical processes have to be understood in detail which is enlightened by some publications (5-8). In this contribution, a multiphysics model for three types of electrolysis processes (steam, CO_2 and co-electrolysis) is presented and evaluated. Relevant parameters like the exchange current density or the anodic / cathodic transfer coefficient including parameter variations for the inlet gas stream, flow rate of the gas, temperature and applied current are investigated. For the microscale properties in the functional layer, Focused Ion Beam Scanning Electron Microscopy (FIB-SEM) is used with the "Slice and View" technique (9,10). Extracting information like the Triple Phase Boundary Length (TPBL), the fraction of electronic and ionic conductive phases, if applicable, or the porosity and tortuosity of the $(La,Sr)CoO_{3-\delta}$ (LSC) air electrode and the Ni – 8 mol% yttria stabilized zirconia (Ni-8YSZ) fuel electrode help in enhancing the simulation quality of high-temperature Solid Oxide Cell (SOC) model. A conversion from the TPBL to an active area to volume ratio for the computation is needed.

Calculated iV-characteristics and experimental curves are compared and serve as a validation for (i,V) data points at higher currents. Depending on the degree of agreement, the (missing) main contributions to loss mechanisms can be identified and initiate a feedback loop for material optimization. Sensitivity analyses are carried out for parameters that are difficult to vary in experiments (e.g. porosity). Porosity and tortuosity parametrize the porous structure for a homogeneously distributed property assumption across the material layers. The ratio between electronic and ionic conductive phase in a cermet fine-tunes the positioning of iV-characteristics within the potential regime of Ohmic and polarization losses. Calculated electrochemical impedance spectra (EIS) enhance the insight into the theoretical system and may be compared to experimental spectroscopy data via Equivalent Circuit Models (ECM). Calculated data from the model are acquired as in the used experimental setup. As an example, calculated EIS data from steam electrolysis are discussed.

Methodology

Description of the real-scale model

The modeling activities are performed with the commercial software package COMSOL Multiphysics ®, a Finite Element Method (FEM) solver for coupled differential equations. Respective physical and chemical descriptions of each layer are provided in the simplified, real-scale model. The SOC model describes a button cell consisting of an LSC(F) electrode (air electrode), an 8YSZ electrolyte and a Ni-8YSZ electrode (fuel electrode) which is separated into a functional and bulk layer. CO_2 and/or H_2O reduction reaction is considered at the fuel electrode leading to three possible model types of electrolysis processes, CO_2 electrolysis, H_2O electrolysis or co-electrolysis. Current collectors/suppliers can be activated, if necessary, at the respective electrodes, a gas supply is provided orthogonally to the electrode surfaces without the need of a supply channel. The model allows for exploring the parameter matrix by varying feed gas flow rate $\dot{n}$, gas composition expressed in partial pressures $p_{\bullet}$, temperature T, current density i, exchange current density i_0 and charge transfer coefficient $\alpha_{\bullet}$. A detailed description and setup of the model concerning the physical and chemical equations can be found in (11). The model is developed further to the up-to-date geometry as shown in Figure 1 where all presented results originate from. The associated equations for each layer remain as described by the model section in the reference.

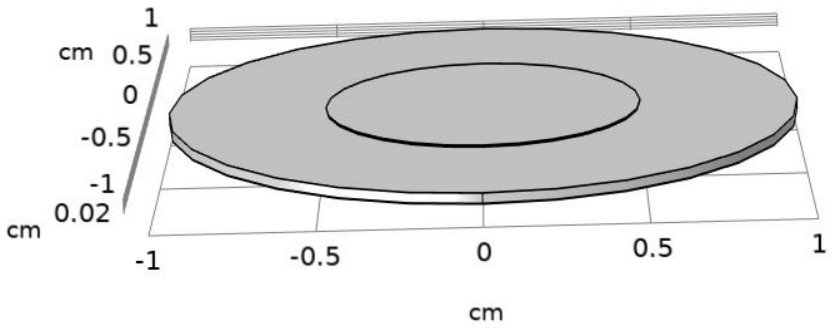

Figure 1. Real-scale model of the high-temperature button cell used in experiments with identical layer thicknesses.

FIB-SEM measurements for structural material properties

For the refinement of modeling data, FIB-SEM measurements for the structural material properties are performed and the results are attributed to the functional layer of the fuel electrode and the entire air electrode. With the Slice and View (S&V) technique a stack of images is recorded with a slice thickness of z = 18 nm. A dual-beam mode allows for evaporation of the 18 nm slice by a Ga^+ source and an electron gun is responsible for the image recording. After fine-tuning of SEM relevant parameters for the image quality an automated slicing and recording is started for a period of approximately 60 hours. During recording, the machine auto-corrects for drift of the sample. Further corrections have to be applied to the whole image stack after recording. Both volumina are taken as representable for the respective electrode layer and add the quantities porosity: ε, tortuosity: τ, active surface to volume ratio: S and share of material ionically conducting: ey to the model. The parameter ey only helps for the description of the fuel electrode as here a phase separation between electronic and ionic conduction occurs. This is not the case for the MIEC LSC(F). An artificial setting of an equal share for electronic and ionic phase conduction in the air electrode ($ey_a = 0.5$) should account for the fact, as the model software otherwise runs into a mathematical problem. Setting this variable does not represent a physical quantity of the system but is a mathematical necessity.

Results and Discussion

Evaluation of the FIB-SEM image stacks

After post-processing of the image stacks for the Ni-8YSZ and the LSC electrode, the reconstructed volume for the fuel electrode was $(21.8 \cdot 18.9 \cdot 9.0)$ µm³ and for the air electrode $(18.0 \cdot 16.9 \cdot 7.2)$ µm³. The results for the Ni-8YSZ electrode can be assigned to its functional layer. That reasons a separate layer within the fuel electrode in the model only accounting for the functional layer properties. In order to separate the respective electronic and ionic conduction phase, an EDX mapping is recorded and the grey scale values associated to the elements Ni and Y/Zr are determined. One example is given in Figure 2. The grey scale intervals allow an automated association for the entire image stack for each element through an algorithm. With the identification, the total amount of Ni and Y/Zr phase is determined in the volume and yields a share of 18% pores, 34% Ni and 48% 8YSZ for the functional layer of the fuel electrode.

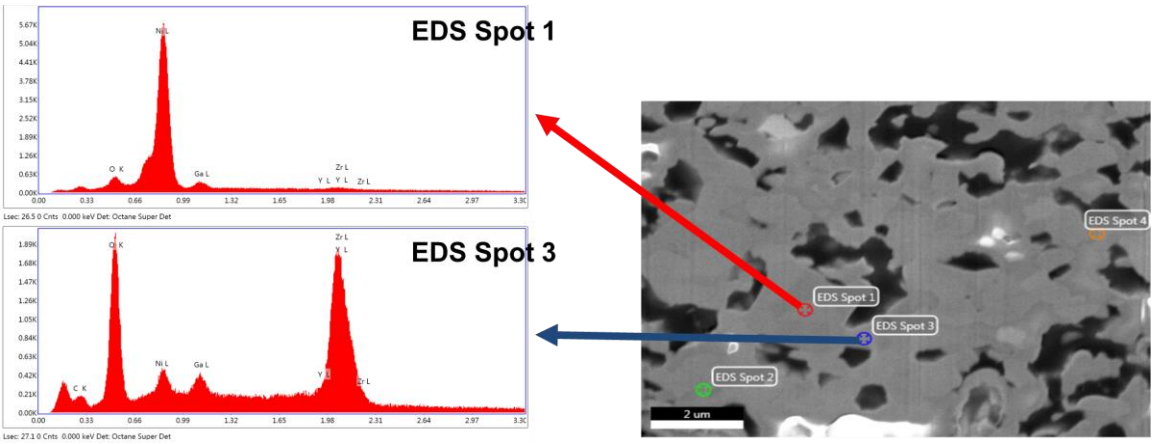

Figure 2. Selected spots for EDX mapping to associate the material affiliation of the region and to generate grey scale intervals for each contributing element.

Especially the porosity of the evaluated functional layer with $\varepsilon_{ff} = 0.18$ differs from the porosity that is observed in the bulk of the electrode ($\varepsilon_f = 0.35$) (12,13). The characterization of the active sites is given by the parameter active surface area to volume ratio. In order to measure this coefficient, the attached area to the voids is calculated and divided by the actual reconstructed volume. The results for both electrodes yield the same order of magnitude: $S_f = 2.1 \cdot 10^6$ m^{-1} respectively $S_a = 5.5 \cdot 10^6$ m^{-1}. The tortuosity for the air electrode is evaluated for each possible direction to $\tau_x = 1.8$, $\tau_y = 2.2$ and $\tau_z = 2.1$. All material parameters contribute to the respective layers in the real-scale model and account for the following presented results of the calculations.

Results from the real-scale model with included material properties

In the following section results from the real-scale model are presented in two measurable quantities: iV characteristics serve as validation for the electrochemical parameters e.g. i_0 and impedance calculations give further insights to the model mechanism. First, iV characteristics together with a sensitivity analysis for some modeling parameters are discussed.

The model is validated for all types of electrolysis. Current-voltage (i,V) pairs for a voltage between 1.4 up to 1.5 V are checked for the respective current density and whether this corresponds to the observations in experiments. In Figure 3, examples for a steam and CO_2 electrolysis are shown with corresponding modeling parameters listed in Table I.

TABLE I. Modeling parameters for the iV characteristics shown in Figure 3.

$i_{0,a}$	$i_{0,f}$ (H_2O)	$i_{0,f}$ (CO_2)	α_a / α_f	p_{H_2O}	p_{CO_2}	p_{H_2}	p_{CO}	T
0.1 A·cm^{-2}	0.4 A·cm^{-2}	0.02 A·cm^{-2}	0.5	50 %	25 %	50 %	10 %	varied
material properties	S_a	S_f	ε_a	τ_a	ε_{ff}	τ_f	ey_a	ey_f
	5.5·10^6 m^{-1}	2.1·10^6 m^{-1}	43 %	1.8	18 %	2.4	0.5	0.48

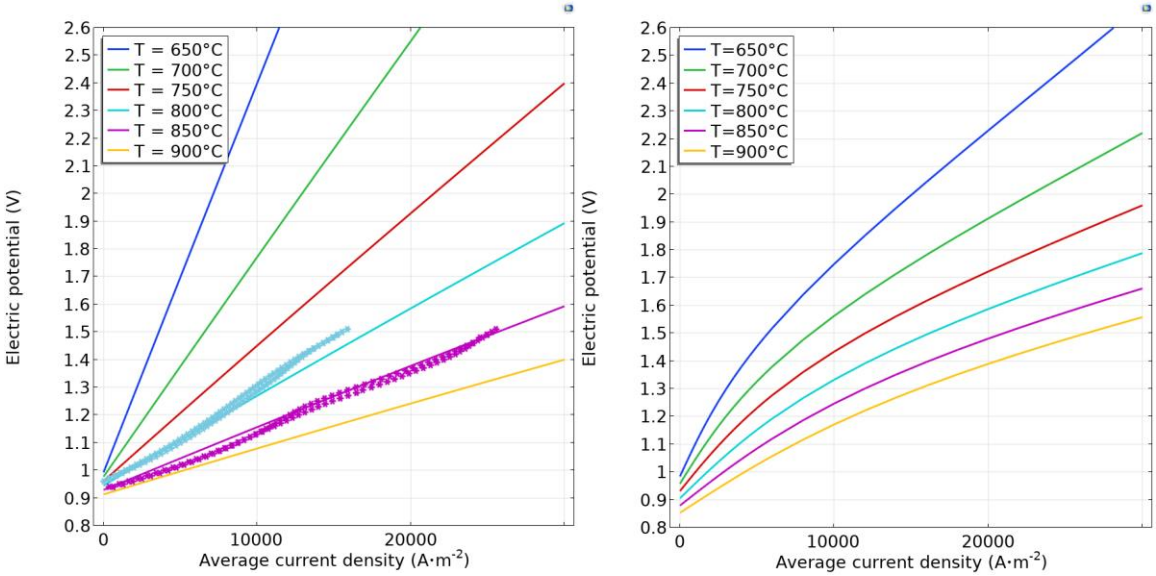

Figure 3. IV characteristics in dependence of temperature for steam and CO_2 electrolysis for benchmarking purposes with corresponding experimental data (asterisks).

The iV characteristics for steam and CO_2 electrolysis show the same trends for the temperature dependence and current-voltage pairs for higher current densities as in experiments. A general assumption is to compare with the best performing cells in experiment. In the case for steam electrolysis for 900 °C, it has been observed that at 1.4 V up to 3 A·cm^{-2} could be achieved with the button cell. With decreasing temperature, the performance decreases as well and lower current densities can be measured at 1.4 V or 1.5 V. The same is true for the CO_2 electrolysis. The (i,V) pairs for higher current densities match with the experimental observations. Overall, the performance is decreased in CO_2 electrolysis and lower current densities are reached at a target voltage of 1.4 V. The contributing loss mechanisms observed in experiment correspond to activation and Ohmic losses. This is the same in the modeled characteristics. Therefore, the order of magnitude for the electrochemical parameter i_0 can be fixed. With $i_{0,f}$ (H_2O) = 0.4 A·cm^{-2} the order of magnitude corresponds to determined values of $i_{0,f}$ (H_2O) from other combined experimental and modeling studies (14). In CO_2 electrolysis, $i_{0,f}$ (CO_2) = 0.02 A·cm^{-2} comes with one order of magnitude lower as compared to the case for steam electrolysis. The electrochemical details are settled for the given framework. It is possible to check now which parameters do actually need to be varied or not to fill the parameter matrix of each high-temperature electrolysis process.

TABLE II. Modeling parameters for the iV characteristics shown in Figure 4.

$i_{0,a}$	$i_{0,f}$ (H_2O)	$i_{0,f}$ (CO_2)	α_a / α_f	p_{H_2O}	p_{CO_2}	p_{H_2}	p_{CO}	T
0.1 A·cm^{-2}	0.4 A·cm^{-2}	0.1 A·cm^{-2}	0.5	12 %	12 %	10 %	10 %	900 °C
material properties	S_a	S_f	ε_a	τ_a	ε_{ff}	τ_f	ey_a	ey_f
	5.5·10^6 m^{-1}	2.1·10^6 m^{-1}	43 %	1.8	18 %	2.4	0.5	0.48

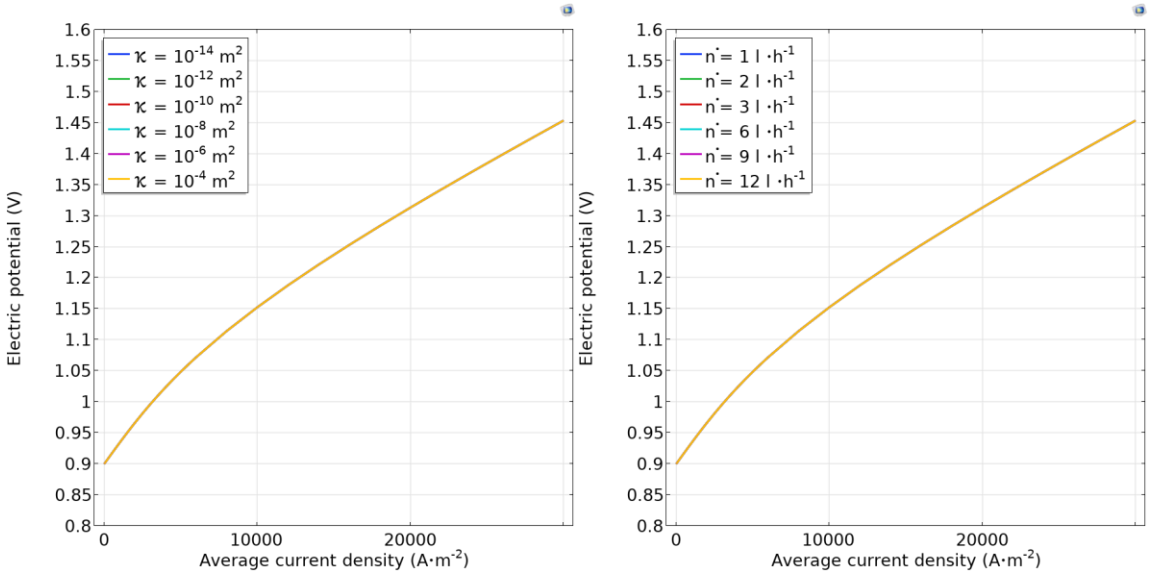

Figure 4. IV characteristics for a sensitivity analysis of gas permeability κ and feed gas flow rate $\dot{n}$ within co-electrolysis.

As shown in Figure 4 with corresponding parameter settings in Table II, a sensitivity analysis for the parameter gas permeability κ and feed gas flow rate $\dot{n}$ is performed. For both, the iV characteristics do not change in shape and magnitude and thus are not sensitive in the given model framework. This means that future calculations do not necessarily have to be checked for variations in these two parameters in the given framework. In the next step, extreme conditions are investigated whether the model is able to also reflect diffusion losses at high current densities.

TABLE III: Modeling parameters for the iV characteristics shown in Figure 5.

$i_{0,a}$		$i_{0,f}$ (CO_2)	α_a / α_f		p_{CO_2}		p_{CO}	
0.1 A·cm^{-2}		0.1 A·cm^{-2}	0.5		18 %		10 %	
material properties	S_a	S_f	ε_a	τ_a	ε_{ff}	τ_f	ey_a	ey_f
	varied	2.1·10^6 m^{-1}	43 %	1.8	18 %	2.4	0.5	0.48

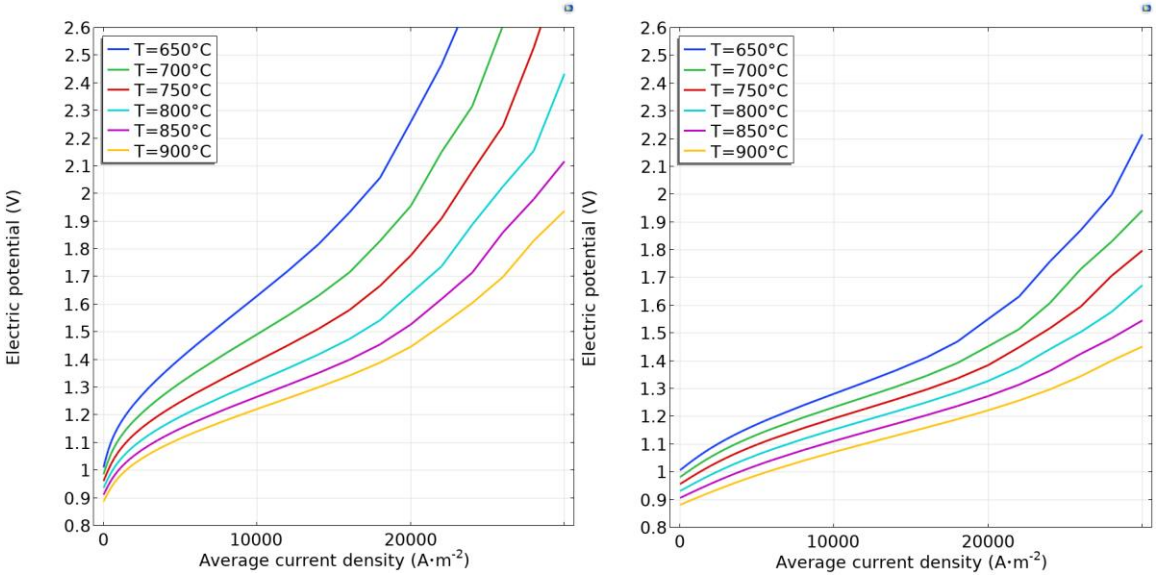

Figure 5. IV characteristics for CO_2 electrolysis with a temperature variation and a variation in the active area to volume ratio (left $S_a = 10^4$ m^{-1}, right: $S_a = 10^5$ m^{-1}).

Diffusion losses can be observed in the model. As an example, the case of CO_2 electrolysis is considered. By reducing the amount of available CO_2 and by decreasing the parameter $S_\bullet$, the characteristics show an increasing change in voltage increase at higher current densities. This is a behavior for dominant diffusion losses. With the selected graphs in Figure 5 with the modeling parameters and conditions given in Table III, it is demonstrated that the model can account for any type of loss mechanism that might occur within experiments as well. From that point onwards, the given framework can be further investigated by means of EIS calculations. The idea is that the model shows limitations and possible bottleneck reactions where further refinement of the given framework can occur.

TABLE IV. Modeling parameters to the EIS characteristics shown in Figure 6.

$i_{0,a}$	$i_{0,f}$ (H_2O)		α_a / α_f	p_{H_2O}		p_{H_2}		T
0.1 A·cm^{-2}	0.4 A·cm^{-2}		0.5	50 %		50 %		varied
material properties	S_a	S_f	ε_a	τ_a	ε_{ff}	τ_f	ey_a	ey_f
	5.5·10^6 m^{-1}	2.1·10^6 m^{-1}	43 %	1.8	18 %	2.4	0.5	0.48

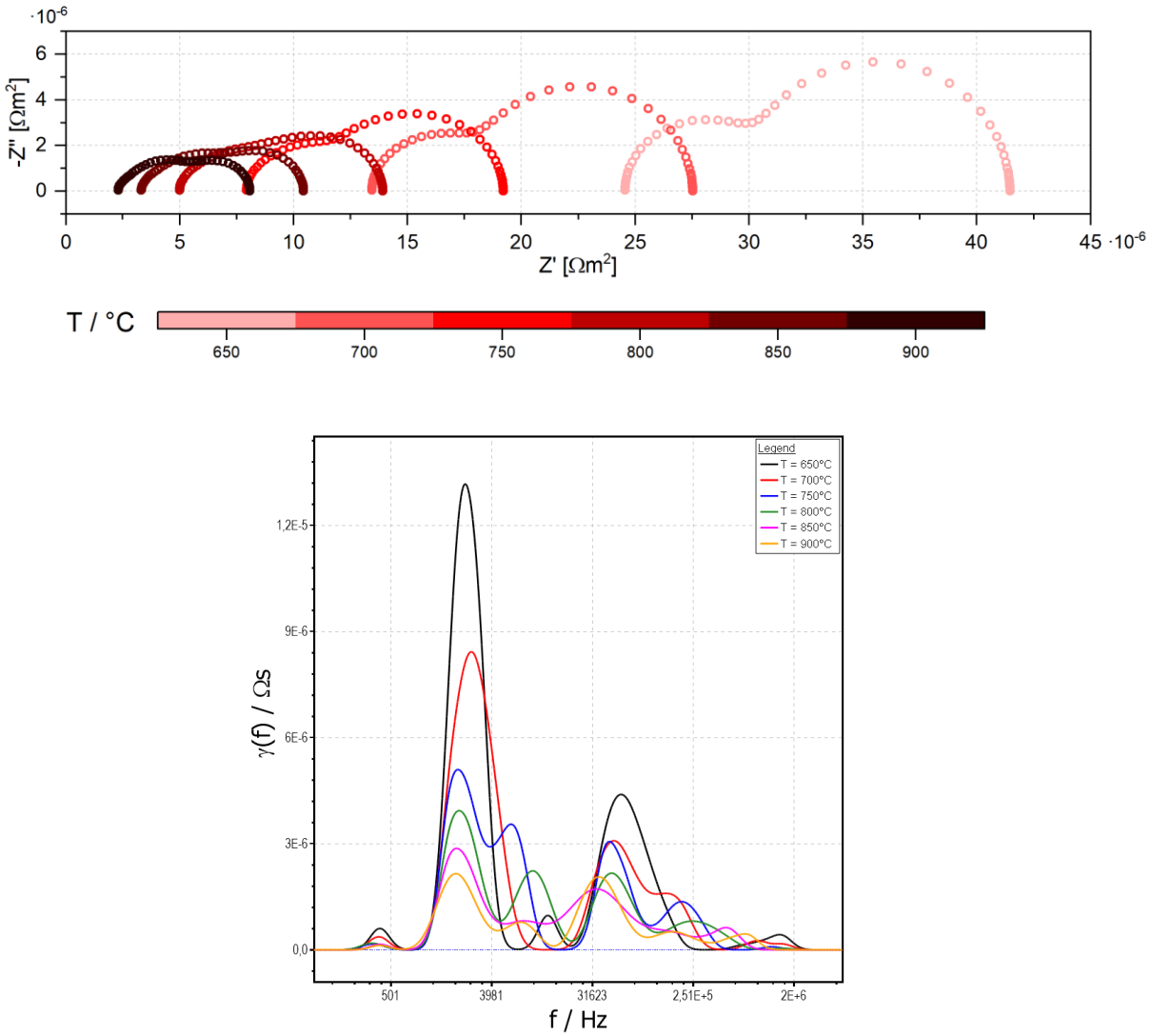

Figure 6. Calculated EIS spectra for steam electrolysis (top) with corresponding DRT spectra (bottom) for a temperature variation with otherwise constant modeling parameters.

EIS calculations are performed and exemplarily discussed for the steam electrolysis case. Figure 6 shows a temperature variation of impedance spectra for steam electrolysis with conditions and parameters given in Table IV. The spectra are recorded with ten points per decade within a frequency range of $[10^{-2}, 10^{7}]$ Hz and at OCV conditions. With increasing temperature, the main peak at 650 °C starts to split into two peaks. While the splitted lower peak tends to shift to higher frequencies until 800 °C, it shifts back with a further increase in temperature. The second peak at 650 °C also splits with increasing temperatures but keeps the frequency shift to higher frequencies for the smaller splitted peak with increasing temperature. It is not clear yet which electrode is responsible for the shift of the peaks with a variation in temperature. In order to separate the contributions from the air and fuel electrode, the orders of magnitude for capacitive contributions of the layers should differ by one. With that, the peaks can be associated to either electrode by comparing them to calculations with equal capacitive contributions. After identifying the correct association, further parameter variations can follow e.g. variations in i_0 to determine the respective contribution of each of the electrodes to the shift. This is still under investigation.

Conclusion

The contribution discusses a real-scale model for all types of high-temperature electrolysis processes. The electrochemical parameter i_0 for steam electrolysis is shown to be of the same order of magnitude as determined from experiments. For CO_2 electrolysis, i_0 is one order of magnitude lower to be able to meet the (i,V) pair values at higher current densities in experiments. The combined case co-electrolysis is also computable. Non-sensitive parameters to performance descriptions are the flow rate and the gas permeability. They can be neglected when going along the parameter matrix of the process. Further insights are given by EIS calculations from the model. An assignment of DRT peaks to either electrode will be possible in future. Further parameter variations will allow for an estimation of the contribution to peak shifts from each electrode.

Acknowledgments

The authors gratefully acknowledge funding by the German Federal Ministry of Education and Research (BMBF) within the Kopernikus Project P2X: Flexible use of renewable resources – research, validation and implementation of 'Power-to-X' concepts (FKZ 03SFK2Z0) and the iNEW Project: incubator sustainable renewable value chains (FKZ 03SF0589).

References

1. A. Hauch[+], R. Küngas[+], P. Blennow, A.B. Hansen, J.B. Hansen, B.V. Mathiesen, and M.B. Mogensen, *Science* **370**, 6513 (2020)
2. S.R. Foit, L. Dittrich, T. Duyster, I.C. Vinke, R.-A. Eichel, and L.G.J. de Haart, *Processes* **8**(11), 1390 (2020)
3. S.R. Foit, I.C. Vinke, L.G.J. de Haart, and R.-A. Eichel, *Angew. Chem. Int. Edit.* **56**(20), 5402 (2017)
4. Y. Tanaka, M.P. Hoerlein, and G. Schiller, *Int. J. Hydrogen Energ.* **41**, 752 (2016)
5. S.E. Wolf, L. Dittrich, M. Nohl, T. Duyster, I.C. Vinke, R.-A. Eichel, and L.G.J. de Haart, *J. Electrochem. Soc.* **169**, 034531 (2022)
6. I.D. Unachukwu, V. Vibhu, I.C. Vinke, R.-A. Eichel, and L.G.J. de Haart, *Energies* **15**, 2136 (2022)
7. C. Mebrahtu[+], M. Nohl[+], L. Dittrich, S.R. Foit, L.G.J. de Haart, R.-A. Eichel, and R. Palkovits, *ChemSusChem* **14**, 2295 (2021)
8. L. Dittrich, M. Nohl, E.E. Jaekel, S.R. Foit, L.G.J. de Haart, and R.-A. Eichel, *J. Electrochem. Soc.* **166**(13), F971 (2019)
9. J.R. Wilson, W. Kobsiriphat, R. Mendoza, H. Chen, J.M. Hiller, D.J. Miller, K. Thornton, P.W. Voorhees, S.B. Adler, and S.A. Barnett, *Nat. Mater.* **5**, 541 (2006)
10. D. Gostovic, J.R. Smith, D.P. Kundinger, K.S. Jones, and E.D. Wachsman, *Electrochem. Solid St.* **10**(12), B214 (2007)
11. M. Nohl, J. Mazumder, I.C. Vinke, R.-A. Eichel, and L.G.J. de Haart, *ECS Trans.* **103**(1), 797 (2021)

12. V. Menon, Q. Fu, V. M. Janardhanan, and O. Deutschmann, *J. Power Sources* **274**, 768 (2015)
13. S. Dierickx, J. Joos, A. Weber, and E. Ivers-Tiffée, *Electrochim. Acta* **265**, 736 (2018)
14. J. Aicart, J. Laurencin, M. Petitjean, and L. Dessemond, *Fuel Cells* **14**(3), 430 (2014)